Efficient Modeling and Systematic Design of Enhanced Phase-Locked Loop Structures

Masoud Karimi-Ghartemani, *Senior Member, IEEE*, Houshang Karimi, *Senior Member, IEEE*, S. Ali Khajehoddin, *Senior Member, IEEE*, and Seyed Milad Hoseinizadeh, *Student Member, IEEE*

***Abstract*—This article presents approaches for efficient modeling and systematic design of enhanced phase-locked loop (ePLL) structures. While different ePLL structures have found a wide acceptance for various applications, their modeling and design aspects have not been fully and systematically reported in the existing literature. This article fills this gap by presenting an effective modeling approach for both the single- and three-phase ePLLs. The models are derived with a view to minimize the number of parameters to be adjusted to simplify the design. The models are then used to develop systematic design algorithms for their parameters. As an example, application of the ePLL in a grid-connected inverter is formulated and studied through simulation and experimental results. The design and simulation files are made available.**

***Index Terms*—Enhanced phase-locked loop (ePLL), phase-locked loop (PLL), PLL design, PLL modeling, unified three-phase signal processor, voltage-source converter (VSC).**

I. Introduction

A PHASE-LOCKED loop (PLL) is a key element of almost all grid-connected power electronic converters. It tracks the grid voltage and provides a reference for synchronization. The PLL is nonlinear due to the nonlinear relationship of the frequency and angle to the sinusoidal waveform. Therefore, its efficient modeling for design and stability analysis is a challenge. A well-designed PLL can significantly improve the responses of the converter and the entire system [1], [2].

The enhanced phase-locked loop (ePLL) was first proposed in [3] and [4] in a single-phase form and then in [5] and [6] in a three-phase form. Its extensions are published in a number of technical papers, e.g., [7]–[10], and a monograph [11]. The single-phase ePLL (1ePLL) removes the historical double-frequency ripples and provides a direct estimation of magnitude in addition to the frequency and angle. The three-phase ePLL (3ePLL), also called unified three-phase signal processor in some studies [12], separates the sequence components and estimates their attributes. Some further extensions include estimation of dc component [9], harmonics and interharmonics [13], synchrophasors [14], [15], and fault analysis [16].

A brief review of some other ePLL-related publications is as follows. Application of the delay signal cancellation approach to the ePLL to remove harmonic and dc components is reported in [17] and [18]. The two-phase version of the ePLL introduced in [19] does not address the unbalanced situations, as further analyzed in [20]. The ePLL's applications in dynamic voltage restorer [21], unified power quality conditioner [22], static compensator [23], [24], microgrids [25]–[27], multilevel inverter [28], synchrophasors [29], grid-connected converters [30]–[33], uninterruptible power supply [34], and voltage flicker mitigation [35], among others, have been reported.

Given the widespread interest in the ePLL, developing simple and workable models for the following objectives is needed: 1) Obj_1: design of the ePLL parameters itself; 2) Obj_2: stability analysis of the entire system wherein the ePLL is adopted; and 3) Obj_3: design of the controllers for such systems while including PLL dynamics. A large-signal linear time-invariant (LTI) model for the 1ePLL has been proposed in [8], where the frequency dynamics are ignored. A similar model for the two-phase ePLL has recently been proposed in [10]. The single-phase model is used to enhance the controller of a converter connected to weak grids [1]. A linear time-periodic (LTP) model for the 1ePLL is presented in [36] with more accurate prediction of its responses and stability margins. A comprehensive and compact rendering of the models (in the form of a single and homogenous presentation) for design and analysis of both the 1ePLL and the 3ePLL is still needed and missing.

This article fills the mentioned gap. It first shows that the combination of two models, i.e., 1) the large-signal LTI model without frequency dynamics and 2) the small-signal phase/frequency dynamics, provide an adequate and effective framework to achieve the aforementioned three objectives. Then, using this framework, direct and simple algorithms to design the ePLL parameters are presented. Moreover, two practical aspects have been given special attention: 1) presence of possible offset in the ePLL input and 2) severe grid voltage conditions. Accordingly, the ePLLs are modified to address them, and their models are also modified. Finally, the systematic application of the ePLL in a grid-connected inverter is formulated and studied in detail using

Manuscript received November 19, 2021; revised February 2, 2022; accepted March 1, 2022. Date of publication March 7, 2022; date of current version April 28, 2022. Recommended for publication by Associate Editor H. H.-C. Iu. *(Corresponding author: Houshang Karimi.)*

Masoud Karimi-Ghartemani is with the Department of Electrical and Computer Engineering, Mississippi State University, Mississippi State, MS 39762 USA (e-mail: karimi@ece.msstate.edu).

Houshang Karimi and Seyed Milad Hoseinizadeh are with the Department of Electrical Engineering, Polytechnique Montreal, Montreal, QC H3T 1J4, Canada (e-mail: houshang.karimi@polymtl.ca; seyed-milad.hoseinizadeh@polymtl.ca).

S. Ali Khajehoddin is with the Department of Electrical and Computer Engineering, University of Alberta, Edmonton, AB T6G 2R3, Canada (e-mail: khajeddin@ualberta.ca).

Color versions of one or more figures in this article are available at https://doi.org/10.1109/TPEL.2022.3157267.

Digital Object Identifier 10.1109/TPEL.2022.3157267

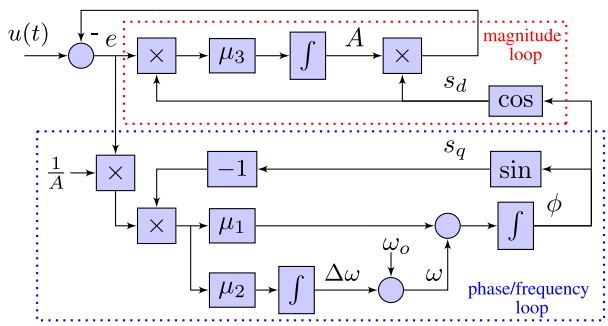

Fig. 1. 1ePLL structure.

computer simulations and experimental results. The design and simulation files are made available.

II. Single-Phase ePLL

Consider a single-phase ac signal $u(t)$ expressed as

$$u(t)=U\cos(\theta)+u_h(t),\quad \theta(t)=\int_0^t \nu(\tau)d\tau+\theta(0) \tag{1}$$

where ν is the fundamental frequency and $u_h(t)$ comprises totality of other components, including dc, harmonics, interharmonics, noise, and transients. The signal $u(t)$ normally represents a measured ac grid voltage. The objective of using a PLL is primarily to detect the unitary synchronizing signal s_d, which is an estimate of $\cos(\theta)$. The quadrature signal s_q is defined as the 90° delayed version of this signal, i.e., s_q estimates $\sin(\theta)$. A PLL may also estimate the magnitude U, the frequency ν, the angle θ, and other parameters within u_h (e.g., dc component, harmonics, etc.).

Fig. 1 shows the structural block diagram of the ePLL, [4], [8], [11]. It provides the direct and quadrature unit vectors s_d and s_q, the magnitude A (estimation of U), the angular frequency ω (estimation of ν), and the phase angle ϕ (estimation of θ). The design parameters μ_1, μ_2, and μ_3 control the transient response of the ePLL. The constant ω_o denotes the rated frequency.

Remark 1: If $u(t)$ is expressed as a sine function, i.e., $u(t)=U\sin(\phi)+u_h(t)$, the block "cos" in Fig. 1 is replaced with "sin" and the block "sin" with "$-\cos$." Then, s_d estimates $\sin(\theta)$ and s_q estimates $-\cos(\theta)$.

Remark 2: The division to A may be replaced with the division by $|A|+\epsilon$ (for a small positive ϵ, such as $0.001A_o$, where A_o is the nominal value of voltage magnitude) to avoid a possible divide-by-zero. The initial value of the A integrator may also be set to A_o for a faster starting.

A. Linear Analysis and Design of 1ePLL

The first main result is given by the following theorem.

Theorem 1: Assume that $\mu_3=\mu_1=\mu$ and $\mu_2=0$. The ePLL of Fig. 1 reduces to a completely LTI system in terms of the state variables $x=[x_1\ x_2]^T=[A\cos(\phi)\ A\sin(\phi)]^T$.

Proof: From Fig. 1, the ePLL's two main equations are as follows:

$$\dot{A}=\mu e\cos(\phi),\quad \dot{\phi}=\omega-\mu\frac{e}{A}\sin(\phi) \tag{2}$$

where $e=u-A\cos(\phi)$. Using $x_1=A\cos(\phi)=As_d$ and $x_2=A\sin(\phi)=As_q$, it is readily seen that

$$\begin{aligned}\dot{x}_1&=\dot{A}\cos(\phi)-A\dot{\phi}\sin(\phi)=\cdots=-\omega x_2+\mu e\\ \dot{x}_2&=\dot{A}\sin(\phi)+A\dot{\phi}\cos(\phi)=\cdots=\omega x_1.\end{aligned} \tag{3}$$

For $\mu_2=0$, i.e., ignoring the dynamics of frequency, (3) reduces to an LTI system with transfer functions

$$X_1(s)=\frac{\mu s}{s^2+\omega_o^2}E(s),\quad X_2(s)=\frac{\mu\omega_o}{s^2+\omega_o^2}E(s) \tag{4}$$

and since $E(s)=U(s)-X_1(s)$, we obtain

$$X_1(s)=\frac{\mu s}{s^2+\mu s+\omega_o^2}U(s),\ X_2(s)=\frac{\mu\omega_o}{s^2+\mu s+\omega_o^2}U(s).$$

This means that at a given frequency, the ePLL's input–output dynamics (the output being $x_1=As_d$) is equivalent to that of a second-order bandpass filter. Thus, its "amplitude/phase" dynamics is characterized by $s^2+\mu s+\omega_o^2=s^2+2\zeta\omega_o s+\omega_o^2=0$ for $\mu=2\zeta\omega_o$.

The second step is to derive a linear model, around the operating point, for the "phase/frequency" dynamics of the ePLL. Let $u(t)=U\cos(\theta)$ and $\theta=\omega_o t$; then, $e=u-A\cos(\phi)=U\cos(\theta)-A\cos(\phi)$, and

$$\dot{\Delta\omega}=-\frac{\mu_2}{A}[U\cos(\theta)-A\cos(\phi)]\sin(\phi)\approx\frac{\mu_2\,U}{2\,A}\sin(\theta-\phi) \tag{5}$$

where the term $-\frac{\mu_2\,U}{2\,A}\sin(\theta+\phi)+\frac{\mu_2}{2}\sin(2\phi)$ is ignored. This high-frequency (double-frequency) term goes to zero as A and ϕ approach U and θ. Similarly, for the angle

$$\dot{\phi}\approx\omega_o+\Delta\omega+\frac{\mu U}{2\,A}\sin(\theta-\phi). \tag{6}$$

Denote $\phi=\omega_o t+\Delta\phi$; then, (5) and (6) may be written as

$$\dot{\Delta\omega}\approx-\frac{\mu_2\,U}{2\,A}\sin(\Delta\phi),\quad \Delta\dot{\phi}\approx\Delta\omega-\frac{\mu U}{2\,A}\sin(\Delta\phi). \tag{7}$$

Linearizing around $(A,\Delta\omega,\Delta\phi)=(U,0,0)$ leads to

$$\dot{\Delta\omega}\approx-\frac{\mu_2}{2}\Delta\phi,\quad \Delta\dot{\phi}\approx\Delta\omega-\frac{\mu}{2}\Delta\phi. \tag{8}$$

Therefore, the phase/frequency dynamics is characterized by $s^2+0.5\,\mu s+0.5\,\mu_2=0$. This can be written as $s^2+2\xi\omega_n s+\omega_n^2=0$, which leads to $\mu_2=\frac{\mu^2}{8\xi^2}$. Since the frequency does not experience very fast changes in a power system, the responses will be more robust if this dynamics is overdamped, i.e., $\xi>1$. For instance, for $\xi=\frac{2}{\sqrt{3}}$, $\mu_2=\frac{3\mu^2}{32}$, and the poles are at $-\frac{3}{8}\mu$ and $-\frac{1}{8}\mu$.

Remark 3: It is concluded from (2) and (7) that the ePLL has two equilibrium points: $(A,\omega,\phi)=(U,\nu,\theta)$ and $(A,\omega,\phi)=(-U,\nu,\theta+\pi)$. Linearizing around the second equilibrium point, i.e., $(A,\Delta\omega,\Delta\phi)=(-U,0,\pi)$, leads to the same dynamics as (8), meaning that both equilibrium points are stable. As a result, the response can converge to negative magnitude and 180° shifted angle. This is not practically an issue because

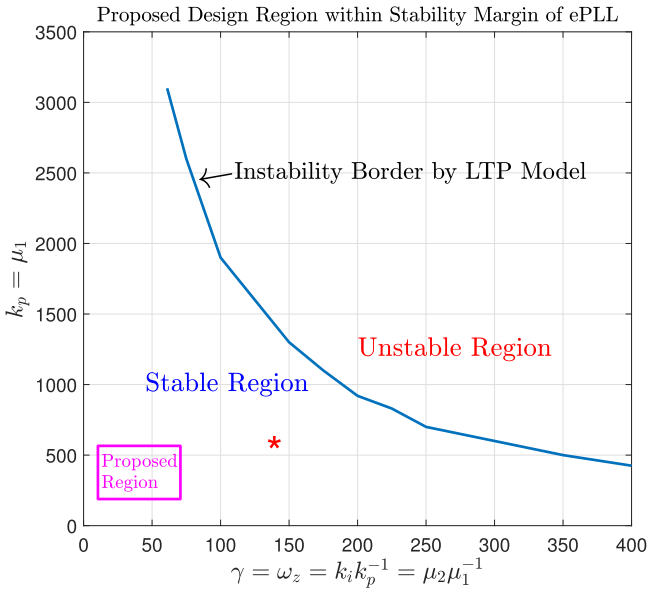

Fig. 2. Proposed design region (inside the box) and the stable region of the ePLL according to the LTP model of [37].

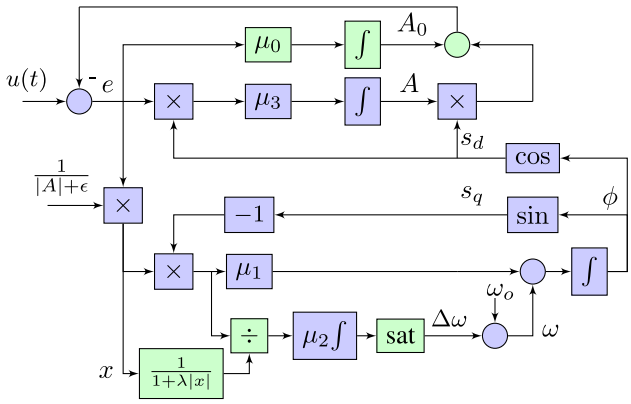

Fig. 3. Modified ePLL to improve its disturbance response.

negative A can be used as a flag to adjust the 180° shift in the angle. However, to completely prevent this problem and also to avoid possible division by zero, the term $\frac{1}{A}$ may be modified to $\frac{1}{|A|+\epsilon}$ for a small positive ϵ, such as $\epsilon = 0.001U_o$, where U_o is the rated magnitude of the input signal. This will force the second equilibrium point to become unstable.

Algorithm I: Design of 1ePLL.

Step 1: Choose $\mu = 2\zeta\omega_o$, where ζ is a damping ratio and ω_o is the system's rated frequency. The recommended range for ζ is $0.25 \le \zeta \le 0.75$. Smaller ζ leads to stronger filtering capability but slower response.

Step 2: Set $\mu_3 = \mu_1 = \mu$ and $\mu_2 = \frac{\mu^2}{8\xi^2}$, where ξ is a damping ratio. The recommended range for ξ is $1 \le \xi \le 1.5$. Larger ξ leads to (smaller bandwidth of frequency estimation loop, ω_n, resulting in) a smoother and more robust frequency estimation but at a lower response speed.

Remark 4: The LTP model of [36] and [37] predicts the stability margins of the ePLL. Fig. 2 shows the proposed design region placed within the stable region of the ePLL, as predicted by the LTP model of [37]. The proposed design region is sufficiently away from the stability border. The horizontal axis in this figure is an intermediary variable $\omega_z = \gamma = \frac{k_i}{k_p} = \frac{\mu_2}{\mu_1}$, which is equal to $\frac{\mu^2/8\xi^2}{\mu} = \frac{\zeta}{4\xi^2}\omega_o$ using our notations. The value for $\frac{\zeta}{4\xi^2}$ according to Algorithm I is between $\frac{0.25}{4\times 1.5^2} = 0.0278$ and $\frac{0.75}{4\times 1^2} = 0.1875$. Therefore, the value of ω_z (or γ of [37]), according to Algorithm I, is between $0.0278 \times 377 = 10.5$ and $0.1875 \times 377 = 70.7$. This means that the values of 300 and 1000 selected in [37] for this parameter are very much exaggerated. Even the value of $\mu = 533$, or $\mu = 444$ for the 50-Hz system (corresponding to $\zeta = 0.707$), and $\mu_2 = 71000$, or $\mu_2 = 49000$ for the 50-Hz system (corresponding to $\xi = 0.707$), suggested in several existing publications (marked by $*$ in Fig. 2) is still extreme. While such extreme selection of parameters may exhibit faster PLL dynamic responses, they increase the level of oscillations during dynamic conditions, cause instability when used in a converter connected to a weak grid, and can also reduce the output current quality when the grid voltage is distorted. Moreover, such levels of fast dynamic response are not indeed required for power system applications. This analysis and the graph shown in Fig. 2 also prove that a statement such as "it has a quite narrow stable zone," regarding the ePLL, made in [37], is scientifically incorrect.

B. Modified ePLL

An ePLL must continue to provide an accurate estimate of s_d and s_q during severe conditions, such as the abrupt transients and disturbances of the grid voltage. Moreover, it can often happen that the input to the PLL has a small unknown dc offset, which may have been present in the actual measured input or have been created during the measurement and signal conditioning stage. Fig. 3 shows a modified ePLL to address large transients and dc aspects.

To enhance the performance during severe grid voltage transients, e.g., short-circuit faults, etc., two modifications are made. First, a saturation block is added to keep the frequency deviation between $[-2\pi\Delta f_{\min} \quad 2\pi\Delta f_{\max}]$. Second, the gain μ_2 is made adaptive to $\frac{\mu_2}{1+\lambda\frac{|e|}{|A|+\epsilon}}$ so that it becomes small during an abrupt disturbance, which will prevent the frequency from shifting too much. For $\lambda = 0$, this feature is disabled. A value of $10 < \lambda < 30$ can well improve the ePLL responses during sudden transients [7]. Too big of λ compromises the speed of frequency estimation.

As for the possible dc (offset), a new branch, including a gain μ_0 and an integrator, is added. Here, A_0 will be the estimate of the dc offset. To design μ_0, from Fig. 3 and (4), we obtain the characteristic equation as

$$1 + \frac{\mu_0}{s} + \frac{\mu s}{s^2 + \omega_o^2} = 0 \Rightarrow 1 + \mu_0 \frac{s^2 + \omega_o^2}{s(s^2 + \mu s + \omega_o^2)} = 0$$

with the typical root locus shown in Fig. 4. One option is to have all three poles aligned on a vertical line. The value of μ_0 that aligns all three poles vertically is obtained from the real root of

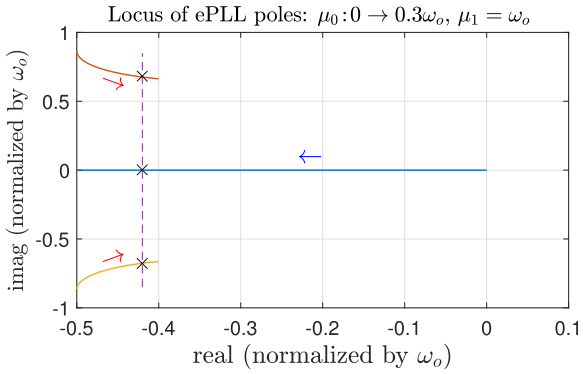

Fig. 4. Locus of ePLL poles when μ_0 varies.

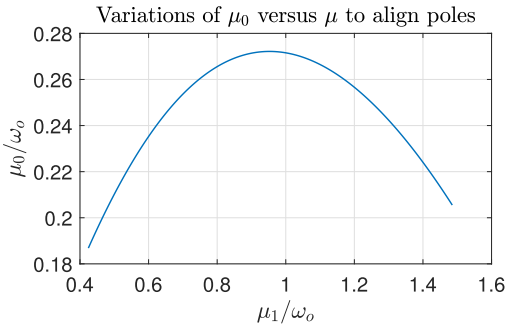

Fig. 5. Variations of μ_0 versus μ for vertically aligned poles.

the equation

$$\bar{\mu}_0^3+3\bar{\mu}_1\bar{\mu}_0^2+(3\bar{\mu}_1^2+9)\bar{\mu}_0+\bar{\mu}_1^3-4.5\bar{\mu}_1=0 \tag{9}$$

where $\bar{\mu}_1=\frac{\mu_1}{\omega_o}$ and $\bar{\mu}_0=\frac{\mu_0}{\omega_o}$. Fig. 5 shows variations of $\bar{\mu}_0$ versus $\bar{\mu}$. It is observed that at $\bar{\mu}=0.95$, we get the maximum value for $\bar{\mu}_0$ at 0.272. At this point, the damping of complex poles is $\zeta=0.5$ and the distance of all three poles to the imaginary axis is $0.405\omega_o$. For a 60-Hz system, this leads to $\mu=360$ and $\mu_0=100$. The ePLL poles will be at -154, $-154\pm j267$. And μ_2 will be $\mu_2=\frac{3}{32}\mu^2=12000$.

Algorithm II: Design of the Modified 1ePLL.

Step 1: Choose the damping ratio ζ and calculate $\mu_1=2\zeta\omega_o$. The recommended range for ζ is $0.25\le\zeta\le 0.75$. Smaller ζ leads to stronger filtering capability but slower response. Set $\mu_3=\mu_1$. (The value of $\zeta=0.475$ may be selected to generate maximum μ_0.)

Step 2: Set $\bar{\mu}_1=\frac{\mu_1}{\omega_o}$ and find the real root of (9) for $\bar{\mu}_0$. Alternatively, use Fig. 5. Set $\mu_0=\omega_o\bar{\mu}_0$. (For $\zeta=0.475$, the maximum value at $\bar{\mu}_0=0.27$ is obtained.)

Step 3: Choose the damping ratio ξ and calculate $\mu_2=\frac{\mu_1^2}{8\xi^2}$. The recommended range for ξ is $1\le\xi\le 1.5$. Larger ξ leads to (smaller bandwidth of frequency estimation loop, ω_n, resulting in) a smoother and more robust frequency estimation but at a lower response speed.

Step 4: Choose $10\le\lambda\le 30$. Larger values of λ results in smoother responses to sudden signal transitions, such as at the start-up or when a grid voltage fault (or abrupt disturbance) occurs. Larger values of λ slows down the frequency adaptivity rate. For $\lambda=0$, this feature is disabled.

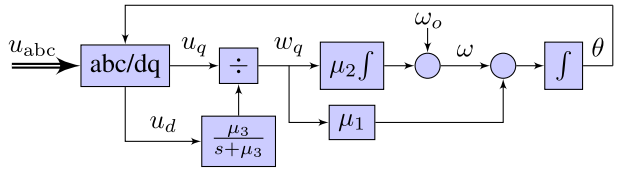

Fig. 6. SRF-PLL with magnitude normalization.

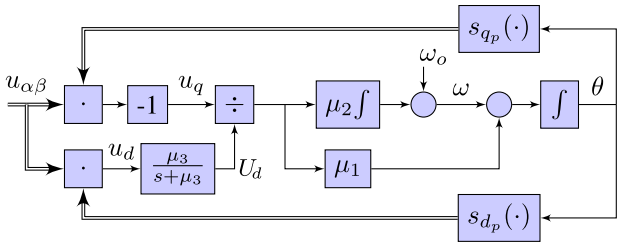

Fig. 7. Alternative presentation of the SRF-PLL of Fig. 6.

III. Three-Phase ePLL

The synchronous reference frame PLL (SRF-PLL) has been commonly used for three-phase applications [38]–[40]. Thus, a brief overview of the SRF-PLL is provided first.

A. Synchronous Reference Frame PLL

The SRF-PLL is shown in Fig. 6, where $u_{abc}(t)$ denotes the three-phase signal, e.g., the measured grid voltage. The variables ω and θ denote the estimated frequency and phase angle, respectively. The two gains μ_1 and μ_2 are the proportional (P) and the integral (I) gains. The direct signal u_d is passed through a simple low-pass filter (LPF) $\frac{\mu_3}{s+\mu_3}$ and is used to normalize the quadrature signal u_q.

Fig. 7 shows an alternative modular representation of the SRF-PLL, where two-phase $\alpha\beta$ representation is used. The vectors s_{d_p} and s_{q_p} are defined as

$$s_{d_p}(\theta)=\begin{bmatrix}\cos(\theta)\\ \sin(\theta)\end{bmatrix},\quad s_{q_p}(\theta)=\begin{bmatrix}\sin(\theta)\\ -\cos(\theta)\end{bmatrix}. \tag{10}$$

The equivalence of Figs. 6 and 7 is readily observed. Fig. 7, however, lends to transition from the SRF-PLL to the ePLL, as explained in the following sections.

For a balanced input, $u_d=U\cos(\phi-\theta)$ and $u_q=U\sin(\phi-\theta)$. Therefore, for θ close to ϕ, w_q may be linearized to $(\phi-\theta)$, and the linearized loop is characterized by

$$1+\left(\mu_1+\frac{\mu_2}{s}\right)\frac{1}{s}=0\Rightarrow s^2+\mu_1 s+\mu_2=0. \tag{11}$$

B. Basic 3ePLL

The basic 3ePLL, shown in Fig. 8, is derived by modifying the SRF-PLL of Fig. 7 through adding a subtraction block at the input, where $e_{\alpha\beta}=u_{\alpha\beta}-U_d s_{d_p}(\theta)$ is performed. The LPF block is also accordingly replaced by an integrator with the gain μ_3. It is readily observed that u_q in the ePLL is identical with u_q in the SRF-PLL. Meanwhile, it can be proved that U_d in the

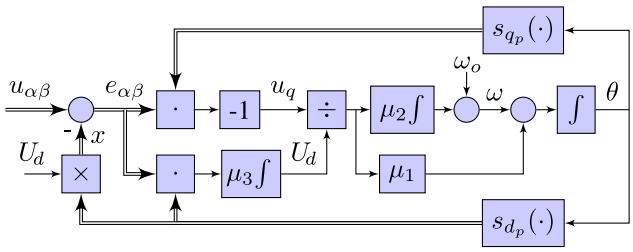

Fig. 8. Basic 3ePLL.

ePLL is also identical with the output of the LPF in the SRF-PLL. Therefore, this ePLL is indeed equivalent to the SRF-PLL. Nevertheless, as we will show, it allows further extensions in a convenient and modular way.

An interesting fact is that a suitable change of variables leads to derive a large-signal LTI representation for the ePLL (or SRF-PLL). This is stated in the following theorem.

Theorem 2: Assume that $\mu_3 = \mu_1$ and $\mu_2 = 0$. The ePLL of Fig. 8 reduces to a completely LTI system in terms of the new state variables $x = [x_1\ x_2]^T = U_d s_{d_p}(\theta)$.

Proof: We first notice that $\omega = \omega_0$ and

$$\dot{\theta} = \omega - \tfrac{\mu_1}{U_d} s_{q_p}(\theta)^T e_{\alpha\beta} = \omega - \tfrac{\mu_1}{U_d}\sin(\theta)e_\alpha + \tfrac{\mu_1}{U_d}\cos(\theta)e_\beta$$
$$\dot{U}_d = \mu_1 s_{d_p}(\theta)^T e_{\alpha\beta} = \mu_1\cos(\theta)e_\alpha + \mu_1\sin(\theta)e_\beta.$$

Differentiating $x_1 = U_d\cos(\theta)$ and $x_2 = U_d\sin(\theta)$ leads to

$$\begin{aligned}\dot{x}_1 &= \dot{U}_d\cos(\theta) - U_d\dot{\theta}\sin(\theta) = -\omega x_2 + \mu_1 e_\alpha\\ \dot{x}_2 &= \dot{U}_d\sin(\theta) + U_d\dot{\theta}\cos(\theta) = \omega x_1 + \mu_1 e_\beta.\end{aligned} \tag{12}$$

Since $e_{\alpha\beta} = u_{\alpha\beta} - x$, we can obtain

$$\dot{x}_1 = -\mu_1 x_1 - \omega x_2 + \mu_1 u_\alpha,\ \dot{x}_2 = \omega x_1 - \mu_1 x_2 + \mu_1 u_\beta. \tag{13}$$

In transfer function form, $X(s) = T(s)U_{\alpha\beta}(s)$, where

$$T(s) = \frac{\mu_1}{(s+\mu_1)^2 + \omega^2}\begin{bmatrix} s+\mu_1 & -\omega \\ \omega & s+\mu_1\end{bmatrix}. \tag{14}$$

This matrix transfer function shows that the PLL uses both the α and β components of the input to generate its outputs. Based on this analysis and (11), a design algorithm may be developed as follows.

Algorithm III: Design of SRF-PLL and Basic 3ePLL.

Step 1: Choose the damping ratio ζ and calculate $\mu_1 = \zeta(1-\zeta^2)^{-0.5}\omega_o \approx 0.25(7\zeta - 1)\omega_o$. The recommended range for ζ is $0.25 \le \zeta \le 0.75$. Smaller ζ leads to stronger filtering capability but slower response. Set $\mu_3 = \mu_1$.

Step 2: Choose the damping ratio ξ and calculate $\mu_2 = \frac{\mu_1^2}{4\xi^2}$. The recommended range for ξ is $1 \le \xi \le 1.5$. Larger ξ leads to (smaller bandwidth of frequency estimation loop, ω_n, resulting in) a smoother and more robust frequency estimation but at a lower response speed.

For example, in a 60-Hz power system, for $\zeta = 0.5$ and $\xi = 1.25$, we get $\mu_1 = 220$ and $\mu_2 = 7600$. The roots of (11) will be at -43 and -177. Primarily, the slower mode (time constant of 23 ms) represents the frequency and the other (time constant of 6 ms) represents the phase angle dynamics, which are quite reasonable.

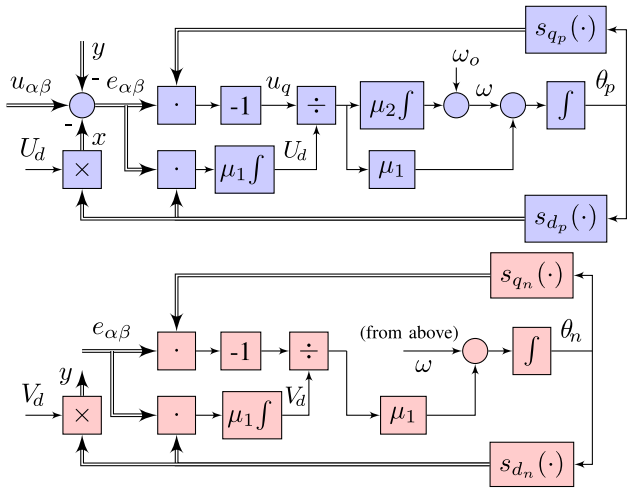

Fig. 9. 3ePLL with negative-sequence estimation/rejection capability.

C. 3ePLL With Negative-Sequence Estimation/Rejection

Fig. 9 shows the ePLL that is upgraded to estimate the negative sequence and reject its impacts on the accuracy of estimated variables. The estimated negative sequence is shown by y. The unit vectors $s_{d_n}(\cdot)$ and $s_{q_n}(\cdot)$ are

$$s_{d_n}(\theta) = \begin{bmatrix}\cos(\theta)\\ -\sin(\theta)\end{bmatrix},\quad s_{q_n}(\theta) = \begin{bmatrix}\sin(\theta)\\ \cos(\theta)\end{bmatrix}. \tag{15}$$

The LTI model of the negative-sequence block is obtained by changing ω to $-\omega$ in the LTI model of the positive-sequence block. Therefore, the state-space equations of the ePLL with negative-sequence estimation are summarized as

$$\begin{aligned}\dot{x}_1 &= -\omega x_2 + \mu_1 e_\alpha,\ \dot{x}_2 = \omega x_1 + \mu_1 e_\beta\\ \dot{y}_1 &= \omega y_2 + \mu_1 e_\alpha,\quad \dot{y}_2 = -\omega y_1 + \mu_1 e_\beta.\end{aligned} \tag{16}$$

Using $e_{\alpha\beta} = u_{\alpha\beta} - x - y$, we obtain

$$\begin{aligned}\dot{x}_1 &= -\mu_1 x_1 - \omega x_2 - \mu_1 y_1 + \mu_1 u_\alpha\\ \dot{y}_1 &= -\mu_1 x_1 - \mu_1 y_1 + \omega y_2 + \mu_1 u_\alpha\\ \dot{x}_2 &= \omega x_1 - \mu_1 x_2 - \mu_1 y_2 + \mu_1 u_\beta\\ \dot{y}_2 &= -\mu_1 x_2 - \omega y_1 - \mu_1 y_2 + \mu_1 u_\beta\end{aligned} \tag{17}$$

which is in the form $\dot{X} = AX + BU$ with the characteristic equation as $\det(sI - A) = (s^2 + 2\mu_1 s + \omega^2)^2$.

Algorithm IV: Design of 3ePLL With Negative Sequence.

Step 1: Choose the damping ratio ζ and set $\mu_1 = \zeta\omega_o$. The recommended range for ζ is $0.25 \le \zeta \le 0.75$. Smaller ζ leads to stronger filtering capability but slower response.

Step 2: Choose the damping ratio ξ and calculate $\mu_2 = \frac{\mu_1^2}{4\xi^2}$. The recommended range for ξ is $1 \le \xi \le 1.5$. Larger ξ leads to (smaller bandwidth of frequency estimation loop, resulting in) a smoother and more robust frequency estimation but at a lower response speed.

For example, in a 60-Hz power system, for $\zeta = 0.5$ and $\xi = 1.25$, we get $\mu_1 = 188$ and $\mu_2 = 5600$. The roots of (11) will be at -37 and -150. Primarily, the slower mode (time constant of 27 ms) represents the frequency and the other (time constant

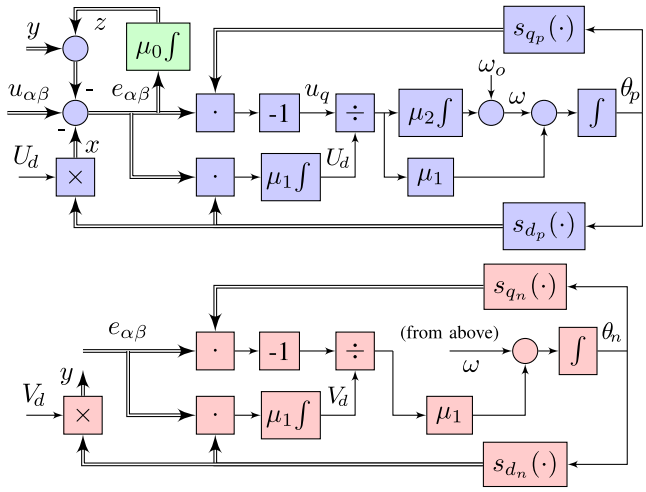

Fig. 10. 3ePLL with negative-sequence and dc estimation/rejection capability.

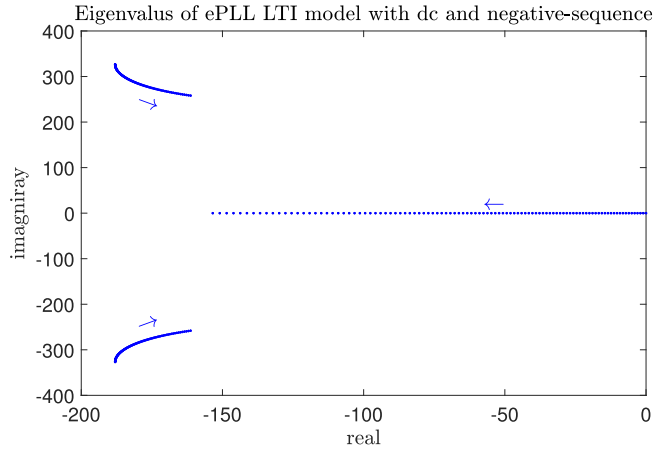

Fig. 11. Poles of the ePLL with dc and negative-sequence rejection loops when μ_0 varies from 0 to 100.

of 7 ms) represents the phase angle dynamics, which are quite reasonable.

D. 3ePLL With Both Negative-Sequence and DC Estimation

Fig. 10 shows a complete version comprising the dc and negative-sequence extraction units. The estimated dc vector is shown by z and the negative sequence by y. Using the two previous ePLLs, the equations of this ePLL are

$$\begin{aligned} \dot{x}_1 &= -\omega x_2 + \mu_1 e_\alpha, & \dot{x}_2 &= \omega x_1 + \mu_1 e_\beta \\ \dot{y}_1 &= \omega y_2 + \mu_1 e_\alpha, & \dot{y}_2 &= -\omega y_1 + \mu_1 e_\beta \\ \dot{z}_1 &= \mu_0 e_\alpha, & \dot{z}_2 &= \mu_0 e_\beta. \end{aligned} \tag{18}$$

On noting that $e_{\alpha\beta} = u_{\alpha\beta} - x - y - z$, we obtain

$$\begin{aligned} \dot{x}_1 &= -\mu_1 x_1 - \omega x_2 - \mu_1 y_1 - \mu_1 z_1 + \mu_1 u_\alpha \\ \dot{x}_2 &= \omega x_1 - \mu_1 x_2 - \mu_1 y_2 - \mu_1 z_2 + \mu_1 u_\beta \\ \dot{y}_1 &= -\mu_1 x_1 - \mu_1 z_1 - \mu_1 y_1 + \omega y_2 + \mu_1 u_\alpha \\ \dot{y}_2 &= -\mu_1 x_2 - \mu_1 z_2 - \omega y_1 - \mu_1 y_2 + \mu_1 u_\beta \\ \dot{z}_1 &= -\mu_0 x_1 - \mu_0 z_1 - \mu_0 y_1 + \mu_0 u_\alpha \\ \dot{z}_2 &= -\mu_0 x_2 - \mu_0 z_2 - \mu_0 y_2 + \mu_0 u_\beta \end{aligned} \tag{19}$$

which represents an LTI system with the A-matrix

$$A = \begin{bmatrix} -\mu_1 & -\omega & -\mu_1 & 0 & -\mu_1 & 0 \\ \omega & -\mu_1 & 0 & -\mu_1 & 0 & -\mu_1 \\ -\mu_1 & 0 & -\mu_1 & \omega & -\mu_1 & 0 \\ 0 & -\mu_1 & -\omega & -\mu_1 & 0 & -\mu_1 \\ -\mu_0 & 0 & -\mu_0 & 0 & -\mu_0 & 0 \\ 0 & -\mu_0 & 0 & -\mu_0 & 0 & -\mu_0 \end{bmatrix}. \tag{20}$$

Algorithm V: Design of 3ePLL With Negative Sequence and DC.

Step 1: Choose the damping ratio ζ and set $\mu_1 = \zeta\omega_o$. The recommended range for ζ is $0.25 \le \zeta \le 0.75$. Smaller ζ leads to stronger filtering capability but slower response.

Step 2: Choose the damping ratio ξ and calculate $\mu_2 = \frac{\mu_1^2}{4\xi^2}$. The recommended range for ξ is $1 \le \xi \le 1.5$. Larger ξ leads to (smaller bandwidth of frequency estimation loop, resulting in) a smoother and more robust frequency estimation but at a lower response speed.

Step 3: Sketch the root locus of A in (20) to find μ_0.

Fig. 11 shows the loci of the eigenvalues of A for $\omega = 377$ rad/s, $\mu_1 = 188$, and $0 \le \mu_0 \le 100$. The poles are repeated. At $\mu_0 = 100$, there are two set of poles at $-161 \pm j258$ and -153, which seems to be a very reasonable design.

Finally, the modifications introduced in the 1ePLL may be applied to the 3ePLL as follows.

Modification 1: The divisions by U_d and V_d may be replaced by $|U_d| + \epsilon$ and $|V_d| + \epsilon$ to prevent division by zero, and to force the second equilibrium point to become unstable.

Modification 2: The gain μ_2 may be divided by $1 + \lambda\frac{||e_{\alpha\beta}||}{|U_d|+\epsilon}$ to reduce transient frequency errors after abrupt input changes. A value of $\lambda = 10$ is suggested and used in this article. For $\lambda = 0$, this feature is disabled.

IV. Application of the ePLL in a Grid-Tied Converter

This section presents a systematic application example of the ePLL for the generation of the current reference in a grid-connected inverter. It is shown how the ePLL can flexibly generate current reference for different scenarios. A current-limiting mechanism is also added to prevent converter overcurrent during low-voltage grid transients.

A. Single-Phase Application

A grid-connected converter executes the real and reactive power set points of P_{set} and Q_{set} via a current control loop. The reference current $i_{\text{ref}}(t)$ must be correctly calculated. For the grid voltage $v_g(t) = V_g\cos\theta$, express the current as

$$i(t) = I\cos(\theta+\varphi) = I_d\cos(\theta) - I_q\sin(\theta) = I_d s_d - I_q s_q.$$

Then, the reference current is computed from

$$i_{\text{ref}} = I_d^{\text{ref}} s_d - I_q^{\text{ref}} s_q, \quad I_d^{\text{ref}} = \frac{2P_{\text{set}}}{V_g}, \; I_q^{\text{ref}} = -\frac{2Q_{\text{set}}}{V_g} \tag{21}$$

where V_g, s_d, and s_q are provided by the ePLL.

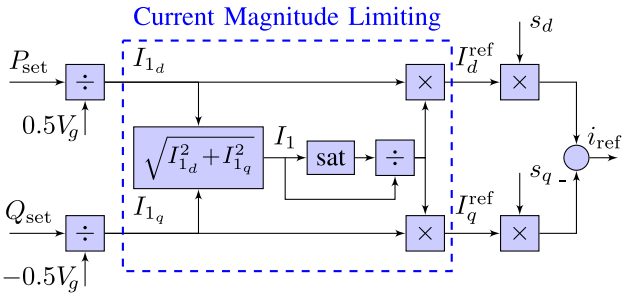

Fig. 12. Generating and limiting single-phase reference.

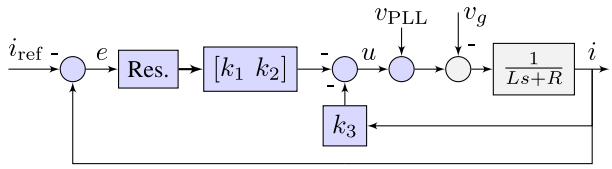

Fig. 13. Current control structure using a resonant controller.

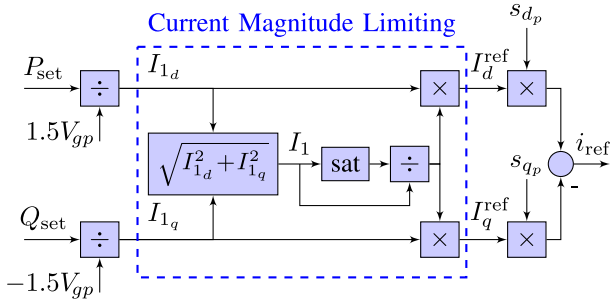

Fig. 14. Generating and limiting (balanced three-phase) reference.

During the transient low-voltage (or short-circuit) grid faults, V_g drops, and as a result, a large current tends to flow to balance the power. To protect the converter, this current must be limited. One approach is shown in Fig. 12. The block denoted by "sat" is a linear saturation block that limits its input within $[0 \quad I_{\max}]$. If the current controller is sufficiently fast, it will keep the converter current close to the reference current and, thus, limit it. The current controller used in this article comprises a resonant controller, as shown in Fig. 13. The feedforward term $v_{\rm PLL} = As_d$ is taken from the ePLL (see Fig. 3).

B. Three-Phase Application

In the three-phase applications, different current reference forms may be used [41]–[43]. For instance, one scenario is to generate a balanced current regardless of whether the grid voltage is balanced or not. Another scenario is to let the current become unbalanced, for example, in order to remove the power ripples [10]. These two scenarios are discussed here.

1) Balanced Current: The current reference generation and limiting mechanism is shown in Fig. 14. Its operation is the same as the one for the single-phase case shown in Fig. 12 except that s_{d_p} and s_{q_p} are vectors here. The reference current $i_{\rm ref}$ is also a vector representing the current in the $\alpha\beta$ domain. To analyze, consider the space-phasor grid voltage expression $\overrightarrow{v_g} = V_{gp}\overrightarrow{s}_{d_p} + V_{gn}\overrightarrow{s}_{d_n}$, where V_{gp} and V_{gn} denote its positive- and negative-sequence magnitudes, and $\overrightarrow{s}_{d_p} = e^{j\theta_p}$ and $\overrightarrow{s}_{d_n} = e^{-j\theta_n}$, in which θ_p and θ_n are total phase angles of positive- and negative-sequence components, respectively. A positive-sequence current can also be expressed as $\overrightarrow{i} = I_d\overrightarrow{s}_{d_p} - I_q\overrightarrow{s}_{q_p}$, where $I_d = I\cos(\varphi)$, $I_q = I\sin(\varphi)$, I is the magnitude, and φ is the phase angle of the current with reference to the voltage. The complex power is defined as $\overrightarrow{S} = 1.5\overrightarrow{v}\,\overrightarrow{i}^{\,*} = P + jQ$ and is calculated as

$$\begin{aligned}&1.5(V_{gp}e^{j\theta_p}+V_{gn}e^{-j\theta_n})(I_de^{-j\theta_p}-I_qe^{-j(\theta_p-\frac{\pi}{2})}) = 1.5V_{gp}I_d\\&-j1.5V_{gp}I_q+1.5V_{gn}I_de^{-j(\theta_p+\theta_n)}-j1.5V_{gn}I_qe^{-j(\theta_p+\theta_n)}\\&= 1.5[V_{gp}I_d + V_{gn}I\cos(\theta_p+\theta_n+\varphi)]\\&+j1.5[-V_{gp}I_q - V_{gn}I\sin(\theta_p+\theta_n+\varphi)] = P + jQ.\end{aligned}$$

This shows that both the real and reactive powers will have double-frequency pulsations if the grid voltage is unbalanced. The current reference (in the $\alpha\beta$ domain) is

$$i_{\rm ref} = I_d^{\rm ref}s_{d_p} - I_q^{\rm ref}s_{q_p},\ I_d^{\rm ref} = \frac{P_{\rm set}}{1.5V_{gp}},\ I_q^{\rm ref} = \frac{-Q_{\rm set}}{1.5V_{gp}}. \quad (22)$$

2) Unbalanced Current: The current is expressed as

$$\overrightarrow{i} = I_{d_p}\overrightarrow{s}_{d_p} - I_{q_n}\overrightarrow{s}_{q_p} + I_{d_n}\overrightarrow{s}_{d_n} - I_{q_n}\overrightarrow{s}_{q_n}$$

where $I_{d_p} = I_p\cos(\varphi_p)$, $I_{q_p} = I_p\sin(\varphi_p)$, $I_{d_n} = I_n\cos(\varphi_n)$, $I_{q_n} = I_n\sin(\varphi_n)$, I_p and I_n are the magnitudes of its positive- and negative-sequence components, respectively, and φ_p and φ_n are their phase angles with reference to the corresponding component of the voltage. The complex power is equal to

$$\begin{aligned}&1.5(V_{gp}\overrightarrow{s}_{d_p}+V_{gn}\overrightarrow{s}_{d_n})(I_{d_p}\overrightarrow{s}_{d_p}-I_{q_p}\overrightarrow{s}_{q_p}+I_{d_n}\overrightarrow{s}_{d_n}-I_{q_n}\overrightarrow{s}_{q_n})^*\\&= 1.5(V_{gp}e^{j\theta_p}+V_{gn}e^{-j\theta_n})(I_{d_p}e^{-j\theta_p}-I_{q_p}e^{-j(\theta_p-\frac{\pi}{2})}+I_{d_n}e^{j\theta_n}\\&-I_{q_n}e^{j(\theta_n-\frac{\pi}{2})}) = 1.5V_{gp}I_{d_p}-j1.5V_{gp}I_{q_p}+1.5V_{gp}I_{d_n}e^{j(\theta_p+\theta_n)}\\&+j1.5V_{gp}I_{q_n}e^{j(\theta_p+\theta_n)}+1.5V_{gn}I_{d_p}e^{-j(\theta_p+\theta_n)}\\&-j1.5V_{gn}I_{q_p}e^{-j(\theta_p+\theta_n)}+1.5V_{gn}I_{d_n}+j1.5V_{gn}I_{q_n}\end{aligned}$$

which is equal to

$$\begin{aligned}&1.5[V_{gp}I_{d_p} + V_{gn}I_{q_n} + V_{gp}I_n\cos(\theta_p+\theta_n+\varphi_n)\\&+V_{gn}I_p\cos(\theta_p+\theta_n+\varphi_p)]+j1.5[-V_{gp}I_{q_p} + V_{gn}I_{q_n}\\&+V_{gp}I_n\sin(\theta_p+\theta_n+\varphi_n) - V_{gn}I_p\sin(\theta_p+\theta_n+\varphi_p)].\end{aligned}$$

It is observed from this expression that it is possible to choose the inverter current to avoid the 2-f pulsations in real power or reactive power individually, but not simultaneously. It is also possible to make a tradeoff between the two, as explained in [41]. One scenario for unbalanced current generation is to remove the 2-f real power oscillations. For this to happen, it is readily seen that the conditions

$$\begin{aligned}&1.5V_{gp}I_p\cos(\varphi_p) + 1.5V_{gn}I_n\cos(\varphi_n) = P_{\rm set}\\&1.5V_{gp}I_p\sin(\varphi_p) - 1.5V_{gn}I_n\sin(\varphi_n) = -Q_{\rm set}\\&\phi_n = \phi_p + \pi,\quad V_{gp}I_n = V_{gn}I_p\end{aligned} \quad (23)$$

must be satisfied. Define the voltage unbalance factor $U_v = \frac{V_{gn}}{V_{gp}}$; then, by combining the equations, we obtain

$$\begin{aligned}&I_{d_p} = \tfrac{P_{\rm set}}{1.5(V_{gp}-U_vV_{gn})},\ I_{q_p} = \tfrac{Q_{\rm set}}{-1.5(V_{gp}+U_vV_{gn})}\\&I_{d_n} = -U_vI_{d_p},\ I_{q_n} = -U_vI_{q_p}.\end{aligned} \quad (24)$$

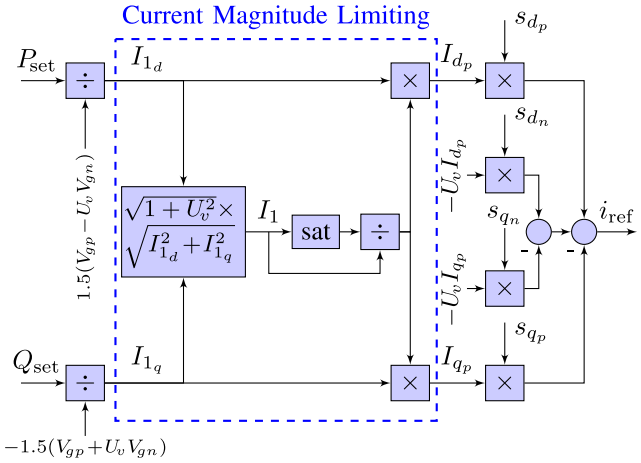

Fig. 15. Generating/limiting (unbalanced three-phase) reference.

TABLE I
SINGLE-PHASE CONVERTER SYSTEM PARAMETERS

Parameter	Symbol	Value	Unit
DC side voltage	V_{dc}	500	V
Grid side voltage (rms)	V_g	240	V
Grid side frequency	f_o (ω_o)	60 (120π)	Hz (rad/s)
Inductance	L	5	mH
Parasitic resistance	R	30	mΩ
Switching frequency	f_{sw}	4	kHz
Power rating	P_{rate}	2	kW
Reactive power rating	Q_{rate}	$\pm$2	kVAr
Current limits	$I_{\text{max, min}}$	$\pm$22	A

The block diagram representation of this current generation mechanism is shown in Fig. 15. Note that the "average magnitude" of the current reference (before limiting) is

$$\sqrt{I_{d_p}^2+I_{q_p}^2+I_{d_n}^2+I_{q_n}^2}=\sqrt{(1+U_v^2)(I_{d_p}^2+I_{q_p}^2)}.$$

This is used to properly adjust the limiting mechanism. This approach limits the average magnitude. The individual phase currents may cross the limits in extremely unbalanced conditions.

C. Simulation Results

1) Single-Phase Grid-Connected Inverter: The system parameters are given in Table I. The controller is designed using the linear quadratic tracker (LQT) approach of [44], leading to the gains of $K=[k_1\ k_2\ k_3]=[7.9\times10^6\ 1.9\times10^4\ 14.9]$. The ePLL of Fig. 3 is used, and its parameters are set at $\mu=360$, $\mu_0=100$, $\mu_2=12000$, $\lambda=20$, and $\Delta f_{\min}=\Delta f_{\max}=5$ Hz, according to Algorithm II. A sample of the inverter responses is shown in Fig. 16. At $t=0.05$ s, the gating commands are applied. Prior to this time, the ePLL is preparing a presynchronization reference for soft start. At $t=0.1$ s, the real power reference of 2 kW is applied. At $t=0.15$ s, the reactive power set point of 2 kVAr and then of -2 kVAr at $t=0.2$ s is applied. The reactive power is restored to 0 at $t=0.25$ s. At $t=0.3$ s, the grid voltage experiences a deep drop of 70% (down to 72 V rms) and restores to normal at $t=0.35$ s. The converter responds by limiting the current at 22 A.

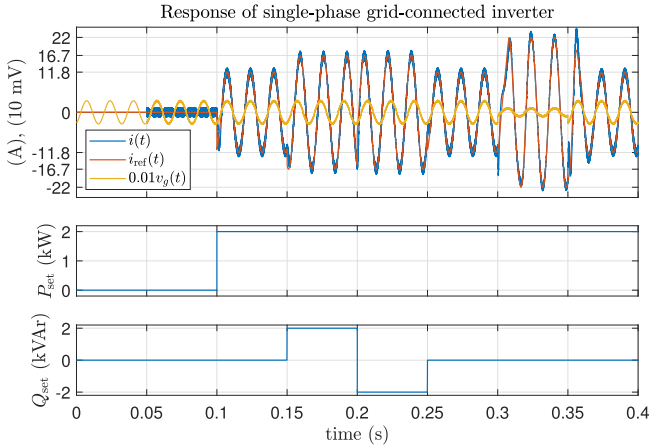

Fig. 16. $t=0$: ePLL starts; $t=0.05$ s: converter starts; $t=0.1$, 0.15, 0.20, 0.25 s: real and reactive power commands; $t=0.3$ s: grid fault (70% deep); and $t=0.35$ s: fault is cleared.

TABLE II
THREE-PHASE CONVERTER SYSTEM PARAMETERS

Parameter	Symbol	Value	Unit
DC side voltage	V_{dc}	500	V
Grid side voltage (rms) (L-G)	V_g	120	V
Grid side frequency	f_o (ω_o)	60 (120π)	Hz (rad/s)
Inductance	L	2	mH
Parasitic resistance	R	20	mΩ
Switching frequency	f_{sw}	4	kHz
Power rating	P_{rate}	10	kW
Reactive power rating	Q_{rate}	$\pm$10	kVAr
Current limits	$I_{\text{max, min}}$	$\pm$70	A

2) Three-Phase Grid-Connected Inverter: The system parameters used in this article are given in Table II. The controller is implemented in the stationary $\alpha\beta$ frame, which comprises two decoupled single-phase channels optimally designed using the LQT approach of [44], leading to the gains of $K=[k_1\ k_2\ k_3]=[3.36\times10^6\ 8\times10^3\ 6]$. The PLL used in this example is the 3ePLL with negative-sequence and dc estimation capability shown in Fig. 10 with the parameters of $\mu_1=188$, $\mu_2=5600$, and $\mu_0=100$ according to Algorithm V.

Three system responses are examined in the next figures: 1) balanced grid voltage and balanced current generation of Fig. 14; 2) unbalanced grid voltage and balanced current generation of Fig. 14; and 3) unbalanced current generation of Fig. 15. At $t=0.05$ s, the gating commands are applied. Prior to this time, the ePLL is preparing a presynchronization reference for soft start. At $t=0.1$ s and $t=0.15$ s, the real and reactive power references of 10 kW and 10 kVAr are applied, respectively. The change of reactive power to 0 and subsequently to -10 kVAr at $t=0.2$ s and $t=0.25$ s are also applied. The reactive power is restored to 0 at $t=0.3$ s. At $t=0.35$ s, the grid voltage experiences a deep drop of 50% (down to about 85 V peak) and restores to normal at $t=0.4$ s. Fig. 17 shows the inverter responses when the grid is balanced and the inverter generates a balanced current according to Fig. 14.

Fig. 18 shows the responses when the grid is unbalanced and the inverter generates a balanced current according to Fig. 14.

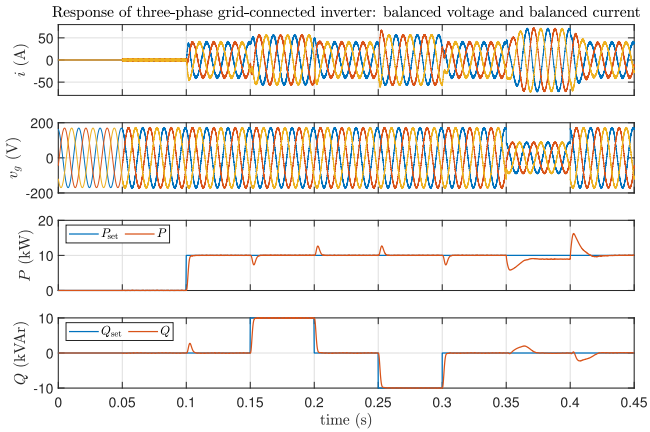

Fig. 17. Generating balanced current while the grid is also balanced. $t = 0$: ePLL starts; $t = 0.05$ s: converter starts; $t = 0.1$, 0.15, 0.20, 0.25, 0.3 s: real and reactive power commands; $t = 0.35$ s: grid fault; and $t = 0.4$ s: fault is cleared.

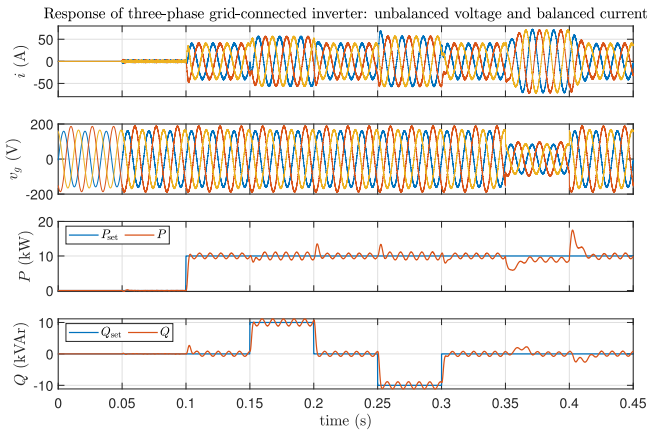

Fig. 18. Generating balanced current while the grid is unbalanced, causing power pulsations.

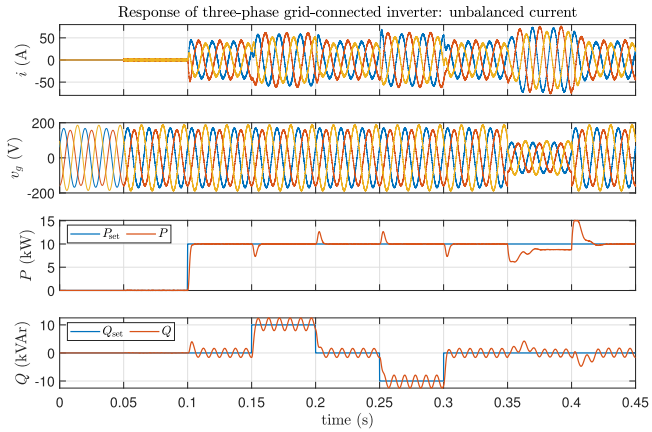

Fig. 19. Generating unbalanced current while the grid is unbalanced, removing real power pulsations.

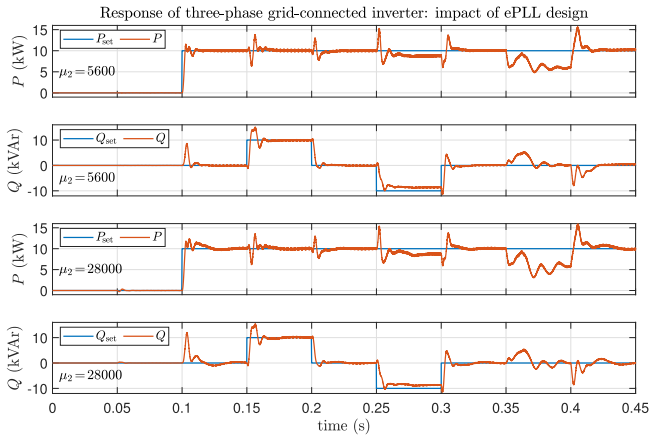

Fig. 20. Responses of three-phase inverter: ePLL designs based on the proposed method ($\mu_2 = 5600$) and the commonly used large value (e.g., $\mu_2 = 28\,000$).

The powers pulsate at double frequency. Fig. 19 shows the responses when the grid is unbalanced and the inverter generates an unbalanced current to remove the real power pulsations according to Fig. 15.

In order to further illustrate the effectiveness of proposed design, Fig. 20 compares the responses of two converters when μ_2 is selected according to our proposal at 5600 and when it is selected at a large value of 28 000 (as it is common to select this gain high). Larger μ_2 causes larger level of oscillations in the powers when the grid is weak.

D. Experimental Results

A hardware-in-the-loop prototype of the three-phase grid-connected VSC is implemented, shown in Fig. 21, to validate the performance of the method described in Section IV-B. The controller is implemented in the OPAL-RT OP5700 field-programmable-gate-array-based real-time simulator. The voltages and currents are measured by the data acquisition unit, OP8660. The converter consists of a three-phase insulated-gate bipolar transistor bridge mounted on a Semikron MiniSkiiP power module with SKHI61 drivers and power rating of 40 kW. The dc-link voltage is set to 240 V, which is provided by a photovoltaic emulator from Chroma. The regenerative grid simulator from Chroma (model 61830) is used as the three-phase grid with a line-to-line voltage of 52 V. The grid frequency is 60 Hz and the L-filter inductance is 5 mH. The data are saved on a PC and are plotted in MATLAB. The control and ePLL settings are the same as those given in Section IV-C2. The current is to be limited at 15 A peak.

The results of two tests are presented, corresponding to two scenarios discussed in Sections IV-B1 and IV-B2, respectively. The responses of the converter to real and reactive power jumps (500 W and 400 VAr at around $t = 0.025$ s and $t = 0.06$ s), a symmetrical low voltage grid fault (50% voltage drop at around $t = 0.1$ s), a single-phase fault (50% voltage drop at $t = 0.3$ s), and a grid frequency jump (2 Hz at $t = 0.5$ s and -2 Hz at $t = 0.65$ s) are shown in Figs. 22 and 23. These extreme grid frequency jumps do not happen in practice and are considered

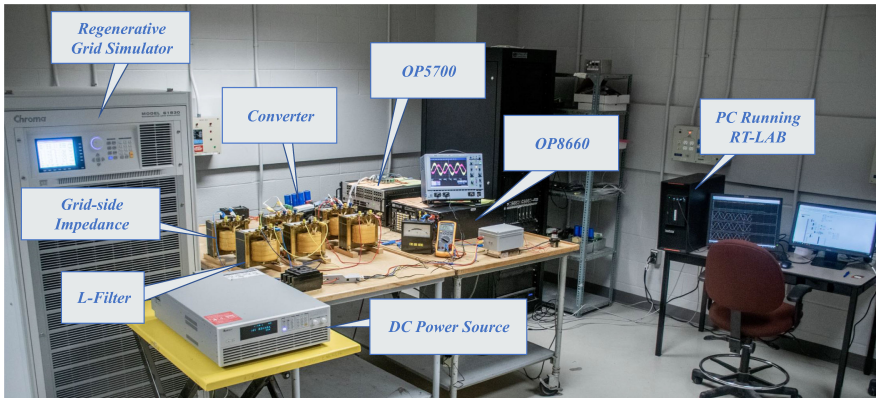

Fig. 21. Photograph of the experimental setup.

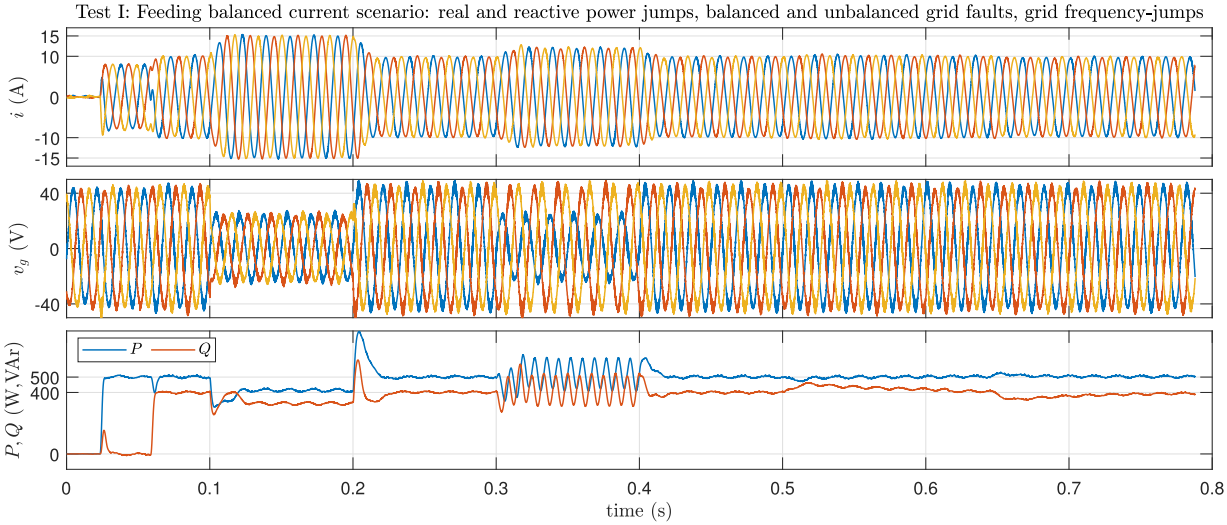

Fig. 22. Experimental results of Test I: feeding balanced current (in response to real and reactive power commands, a symmetrical, and an asymmetrical grid fault, and a ± 2 Hz grid frequency jump.)

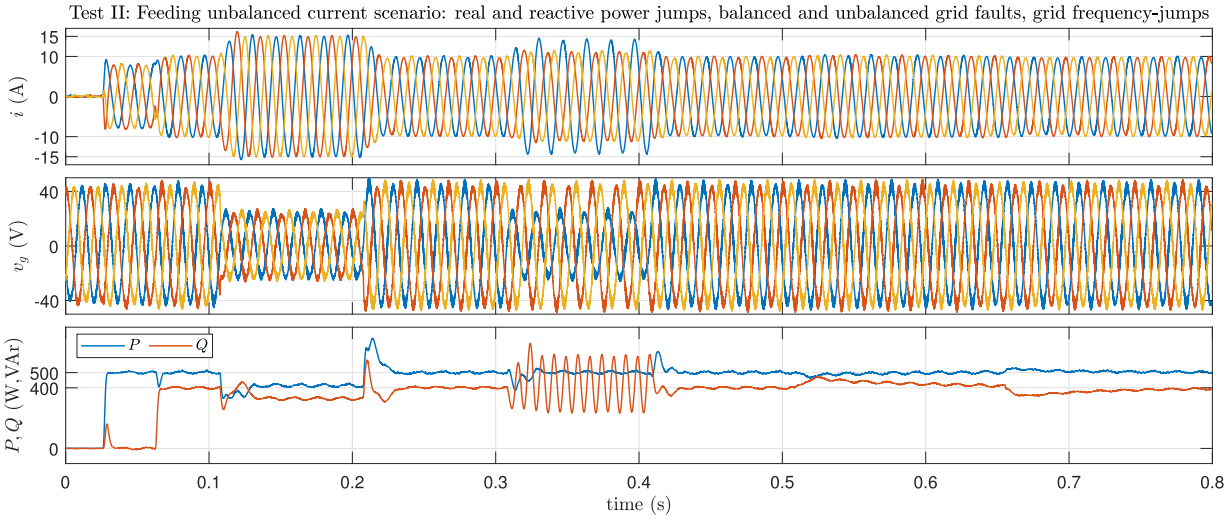

Fig. 23. Experimental results of Test II: feeding unbalanced current (in response to real and reactive power commands, a symmetrical, and an asymmetrical grid fault, and a ± 2 Hz grid frequency jump.)

here only for extreme response analysis. Test I shows the responses of the controller described in Section IV-B1. As shown in Fig. 22, the converter exhibits quick and smooth tracking of power commands, generates balanced current during the fault, and limits its peak to 15 A. Test II shows the responses of the controller described in Section IV-B2. As shown in Fig. 23, the converter shows fast and smooth execution of power commands, generates balanced current during the symmetrical fault and limits its peak to 15 A, and generates unbalanced current during the single-phase fault in a way to remove the double-frequency ripples from the real power. As a result, the reactive power shows larger double-frequency ripples. The sharp grid voltage frequency jumps of ± 2 Hz at $t = 0.5$ s and $t = 0.65$ s only cause a tiny swing in the real and reactive powers. The impact of this large frequency jump on the current waveform is not visible.

V. Conclusion

This article presented an efficient modeling and systematic design of the 1ePLL and 3ePLL concepts. A combination of a large-signal linear model ignoring the frequency dynamics and a small-signal linear model, including the phase/frequency dynamics, was used to effectively analyze and design the ePLL gains. Several step-by-step algorithms to robustly design various ePLLs were derived. The ePLLs were adjusted to address the presence of the dc component and the severe grid voltage conditions. Finally, a grid-connected inverter application was systematically formulated and studied through computer simulations and experimental testing. The design and simulation files are made available.

References

[1] S. Silwal, S. Taghizadeh, M. Karimi-Ghartemani, M. J. Hossain, and M. Davari, "An enhanced control system for single-phase inverters interfaced with weak and distorted grids," *IEEE Trans. Power Electron.*, vol. 34, no. 12, pp. 12 538–12 551, Dec. 2019.

[2] S. Milad Hoseinizadeh, S. Ouni, H. Karimi, M. Karimi-Ghartemani, and K. L. Lian, "Comparison of PLL-based and PLL-less vector current controllers," *IEEE J. Emerg. Sel. Topics Power Electron.*, vol. 10, no. 1, pp. 436–445, Feb. 2022, doi: 10.1109/JESTPE.2021.3066512.

[3] M. Karimi-Ghartemani and M. R. Iravani, "A new phase-locked loop (PLL) system," in *Proc. 44th IEEE Midwest Symp. Circuits Syst.*, 2001, vol. 1, pp. 421–424.

[4] M. Karimi-Ghartemani and M. R. Iravani, "A nonlinear adaptive filter for online signal analysis in power systems: Applications," *IEEE Trans. Power Del.*, vol. 17, no. 2, pp. 617–622, Apr. 2002.

[5] M. Karimi-Ghartemani and H. Karimi, "Analysis of symmetrical components in time-domain," in *Proc. 48th Midwest Symp. Circuits Syst.*, 2005, vol. 1, pp. 28–31.

[6] M. Karimi-Ghartemani and H. Karimi, "Processing of symmetrical components in time-domain," *IEEE Trans. Power Syst.*, vol. 22, no. 2, pp. 572–579, May 2007.

[7] M. K. Ghartemani, S. A. Khajehoddin, P. K. Jain, and A. Bakhshai, "Problems of startup and phase jumps in PLL systems," *IEEE Trans. Power Electron.*, vol. 27, no. 4, pp. 1830–1838, Apr. 2012.

[8] M. Karimi-Ghartemani, "Linear and pseudolinear enhanced phased-locked loop (EPLL) structures," *IEEE Trans. Ind. Electron.*, vol. 61, no. 3, pp. 1464–1474, Mar. 2014.

[9] M. Karimi-Ghartemani, S. A. Khajehoddin, P. K. Jain, A. Bakhshai, and M. Mojiri, "Addressing DC component in PLL and notch filter algorithms," *IEEE Trans. Power Electron.*, vol. 27, no. 1, pp. 78–86, Jan. 2012.

[10] H. Karimi, M. Karimi-Ghartemani, and K. Sheshyekani, "Robust control of three-phase voltage source converters under unbalanced grid conditions," *IEEE Trans. Power Electron.*, vol. 34, no. 11, pp. 11278–11289, Nov. 2019.

[11] M. Karimi-Ghartemani, *Enhanced Phase-Locked Loop Structures for Power and Energy Applications*. Hoboken, NJ, USA: Wiley, 2014.

[12] H. Karimi, A. Yazdani, and R. Iravani, "Negative-sequence current injection for fast islanding detection of a distributed resource unit," *IEEE Trans. Power Electron.*, vol. 23, no. 1, pp. 298–307, Jan. 2008.

[13] M. Karimi-Ghartemani, H. Mokhtari, M. R. Iravani, and M. Sedighy, "A signal processing system for extraction of harmonics and reactive current of single-phase systems," *IEEE Trans. Power Del.*, vol. 19, no. 3, pp. 979–986, Jul. 2004.

[14] M. Karimi-Ghartemani, B.-T. Ooi, and A. Bakhshai, "Application of enhanced phase-locked loop system to the computation of synchrophasors," *IEEE Trans. Power Del.*, vol. 26, no. 1, pp. 22–32, Jan. 2011.

[15] H. Zamani, M. Karimi-Ghartemani, and M. Mojiri, "Analysis of power system oscillations from PMU data using an EPLL-based approach," *IEEE Trans. Instrum. Meas.*, vol. 67, no. 2, pp. 307–316, Feb. 2018.

[16] M. Karimi-Ghartemani and J. A. Walseth, "Using the EPLL algorithm as a preprocessor for fault analysis," in *Proc. 11th Int. Conf. Inf. Sci., Signal Process Appl.*, 2012, pp. 1377–1382.

[17] S. Gude and C.-C. Chu, "Dynamic performance improvement of multiple delayed signal cancelation filters based three-phase enhanced-PLL," *IEEE Trans. Ind. Appl.*, vol. 54, no. 5, pp. 5293–5305, Sep./Oct. 2018.

[18] F. Wu, D. Sun, L. Zhang, and J. Duan, "Influence of plugging DC offset estimation integrator in single-phase EPLL and alternative scheme to eliminate effect of input DC offset and harmonics," *IEEE Trans. Ind. Electron.*, vol. 62, no. 8, pp. 4823–4831, Aug. 2015.

[19] F. Wu, L. Zhang, and J. Duan, "A new two-phase stationary-frame-based enhanced PLL for three-phase grid synchronization," *IEEE Trans. Circuits Syst. II, Express Briefs*, vol. 62, no. 3, pp. 251–255, Mar. 2015.

[20] D. Sun, H. Long, K. Zhou, F. Wu, and L. Sun, "An improved $\alpha\beta$-EPLL based on active disturbance rejection control for complicated power grid conditions," *IEEE Access*, vol. 7, pp. 139276–139293, 2019.

[21] T. A. Naidu, S. R. Arya, and R. Maurya, "Multiobjective dynamic voltage restorer with modified EPLL control and optimized PI-controller gains," *IEEE Trans. Power Electron.*, vol. 34, no. 3, pp. 2181–2192, Mar. 2019.

[22] A. Teke, L. Saribulut, and M. Tumay, "A novel reference signal generation method for power-quality improvement of unified power-quality conditioner," *IEEE Trans. Power Del.*, vol. 26, no. 4, pp. 2205–2214, Oct. 2011.

[23] S. K. Patel, S. R. Arya, R. Maurya, and B. Singh, "Control of distribution static compensator using three-phase enhanced phase-locked loop," *Electr. Power Compon. Syst.*, vol. 44, no. 13, pp. 1515–1529, 2016.

[24] B. Singh and S. R. Arya, "Implementation of single-phase enhanced phase-locked loop-based control algorithm for three-phase DSTATCOM," *IEEE Trans. Power Del.*, vol. 28, no. 3, pp. 1516–1524, Jul. 2013.

[25] S. Gude and C.-C. Chu, "Single-phase enhanced phase-locked loops based on multiple delayed signal cancellation filters for micro-grid applications," *IEEE Trans. Ind. Appl.*, vol. 55, no. 6, pp. 7122–7133, Nov./Dec. 2019.

[26] M. Rezkallah, S. Singh, B. Singh, A. Chandra, H. Ibrahim, and M. Ghandour, "Implementation of two-level coordinated control for seamless transfer in standalone microgrid," *IEEE Trans. Ind. Appl.*, vol. 57, no. 1, pp. 1057–1068, Jan./Feb. 2021.

[27] S. Gholami, M. Aldeen, and S. Saha, "Control strategy for dispatchable distributed energy resources in islanded microgrids," *IEEE Trans. Power Syst.*, vol. 33, no. 1, pp. 141–152, Jan. 2018.

[28] A. Isazadeh, J. Adabi, M. Rezanejad, and M. E. Adabi, "Operation and control of a grid-connected asymmetrical cascaded multilevel inverter," *IEEE Trans. Emerg. Sel. Topics Power Electron.*, vol. 9, no. 2, pp. 1614–1623, Apr. 2021.

[29] P. Kumar and G. Gurrala, "IEEE C37.118.1a-2014 compliance testing of EPLL and DFAC-PLL for synchrophasors," in *Proc. North Amer. Power Symp.*, 2018, pp. 1–6.

[30] B. Singh and S. Sharma, "Design and implementation of four-leg voltage-source-converter-based VFC for autonomous wind energy conversion system," *IEEE Trans. Ind. Electron.*, vol. 59, no. 12, pp. 4694–4703, Dec. 2012.

[31] F. Wu, X. Li, and J. Duan, "Improved elimination scheme of current zero-crossing distortion in unipolar hysteresis current controlled grid-connected inverter," *IEEE Trans. Ind. Informat.*, vol. 11, no. 5, pp. 1111–1118, Oct. 2015.

[32] P. Jain, V. Agarwal, and B. P. Muni, "Hybrid phase locked loop for controlling master-slave configured centralized inverters in large solar photovoltaic power plants," *IEEE Trans. Ind. Appl.*, vol. 54, no. 4, pp. 3566–3574, Jul./Aug. 2018.

[33] S. Kumar, A. K. Verma, I. Hussain, B. Singh, and C. Jain, "Better control for a solar energy system: Using improved enhanced phase-locked loop-based control under variable solar intensity," *IEEE Ind. Appl. Mag.*, vol. 23, no. 2, pp. 24–36, Mar./Apr. 2017.

[34] R. M. Santos Filho, P. F. Seixas, P. C. Cortizo, L. A. Torres, and A. F. Souza, "Comparison of three single-phase PLL algorithms for ups applications," *IEEE Trans. Ind. Electron.*, vol. 55, no. 8, pp. 2923–2932, Aug. 2008.
[35] S. K. Sharma, A. Chandra, M. Saad, S. Lefebvre, D. Asber, and L. Lenoir, "Voltage flicker mitigation employing smart loads with high penetration of renewable energy in distribution systems," *IEEE Trans. Sustain. Energy*, vol. 8, no. 1, pp. 414–424, Jan. 2017.
[36] S. Golestan, J. M. Guerrero, and J. C. Vasquez, "Modeling and stability assessment of single-phase grid synchronization techniques: Linear time-periodic versus linear time-invariant frameworks," *IEEE Trans. Power Electron.*, vol. 34, no. 1, pp. 20–27, Jan. 2019.
[37] S. Golestan, J. Matas, A. M. Abusorrah, and J. M. Guerrero, "More-stable EPLL," *IEEE Trans. Power Electron.*, vol. 37, no. 1, pp. 1003–1011, Jan. 2022.
[38] V. Blasko, J. Moreira, and T. Lipo, "A new field oriented controller utilizing spatial position measurement of rotor end ring current," in *Proc. 20th Annu. IEEE Power Electron. Spec. Conf.*, 1989, pp. 295–300.
[39] S.-K. Chung, "A phase tracking system for three phase utility interface inverters," *IEEE Trans. Power Electron.*, vol. 15, no. 3, pp. 431–438, May 2000.
[40] S. Golestan, J. M. Guerrero, and J. C. Vasquez, "Three-phase PLLs: A review of recent advances," *IEEE Trans. Power Electron.*, vol. 32, no. 3, pp. 1894–1907, Mar. 2017.
[41] F. Wang, J. L. Duarte, and M. A. Hendrix, "Pliant active and reactive power control for grid-interactive converters under unbalanced voltage dips," *IEEE Trans. Power Electron.*, vol. 26, no. 5, pp. 1511–1521, May 2011.
[42] P. Rodriguez, A. Timbus, R. Teodorescu, M. Liserre, and F. Blaabjerg, "Reactive power control for improving wind turbine system behavior under grid faults," *IEEE Trans. Power Electron.*, vol. 24, no. 7, pp. 1798–1801, Jul. 2009.
[43] P. Rodriguez, A. V. Timbus, R. Teodorescu, M. Liserre, and F. Blaabjerg, "Flexible active power control of distributed power generation systems during grid faults," *IEEE Trans. Ind. Electron.*, vol. 54, no. 5, pp. 2583–2592, Oct. 2007.
[44] S. A. Khajehoddin, M. Karimi-Ghartemani, and M. Ebrahimi, "Optimal and systematic design of current controller for grid-connected inverters," *IEEE Trans. Emerg. Sel. Topics Power Electron.*, vol. 6, no. 2, pp. 812–824, Jun. 2018.

Masoud Karimi-Ghartemani (Senior Member, IEEE) received the Ph.D. degree in electrical and computer engineering from the University of Toronto, Toronto, ON, Canada, in 2004.

From 2005 to 2008, he was a Faculty Member with the Department of Electrical Engineering, Sharif University of Technology, Tehran, Iran. From 2008 to 2011, he was a member of ePOWER Laboratory, Queen's University, Kingston, ON, Canada. Since 2012, he has been with the Department of Electrical and Computer Engineering, Mississippi State University (MSU), Mississippi State, MS, USA, where he is currently a Professor. His research interests include modeling and control of distributed and renewable energy systems.

Dr. Karimi is the recipient of the 2020 Faculty Research Award at MSU's Bagley College of Engineering. He is an Associate Editor for the IEEE TRANSACTIONS ON INDUSTRIAL ELECTRONICS, IEEE TRANSACTIONS ON SUSTAINABLE ENERGY, and IEEE POWER AND ENERGY SOCIETY LETTERS.

Houshang Karimi (Senior Member, IEEE) received the Ph.D. degree in electrical engineering from the University of Toronto, Toronto, ON, Canada, in 2007.

From 2009 to 2012, he was an Assistant Professor with the Department of Electrical Engineering, Sharif University of Technology, Tehran, Iran. In 2013, he joined the Department of Electrical Engineering, Polytechnique Montreal, Montreal, QC, Canada, where he is currently an Associate Professor. His research interests include control systems, microgrid control, and smart grids.

S. Ali Khajehoddin (Senior Member, IEEE) received the Ph.D. degree in electrical engineering specialized in power electronics and their applications in renewable energy systems from Queen's University, Kingston, ON, Canada, in 2010.

He cofounded a startup company, which was focused on the development and production of power analyzers and smart metering products used for smart grid applications. For his Ph.D. research with Queen's University, he focused on the design and implementation of compact and durable microinverters for photovoltaic grid-connected systems. Based on this research, Queen's University spun off SPARQ systems, Inc., where he worked on mass production and commercialization of microinverters as the Lead Research and Development Engineer from 2010 to 2013. He joined the Department of Electrical and Computer Engineering, University of Alberta, Edmonton, AB, Canada, in 2013.

Dr. Khajehoddin is an Associate Editor for the IEEE TRANSACTIONS ON POWER ELECTRONICS and IEEE JOURNAL OF EMERGING AND SELECTED TOPICS IN POWER ELECTRONICS.

Seyed Milad Hoseinizadeh (Student Member, IEEE) received the B.Sc. degree from Shahid Chamran University, Ahvaz, Iran, in 2011, and the M.Sc. degree from the K. N. Toosi University of Technology, Tehran, Iran, in 2013, both in electrical engineering. He is currently working toward the Ph.D. degree with the Department of Electrical Engineering, Polytechnique Montreal, Montreal, QC, Canada.

His research interests include control systems, microgrid control, and smart grids.